Biophysical Journal, Volume *122*

Supplemental information

Branched actin cortices reconstituted in vesicles sense membrane curvature

Lucia Baldauf, Felix Frey, Marcos Arribas Perez, Timon Idema, and Gijsje H. Koenderink

Supporting Material:
Branched actin cortices reconstituted in vesicles sense membrane curvature

Lucia Baldauf[1,2,*], Felix Frey[1,3,*], Marcos Arribas Perez[1], Timon Idema[1,†], and Gijsje H. Koenderink[1,**]

[1] Department of Bionanoscience, Kavli Institute of Nanoscience Delft, Delft University of Technology, Van der Maasweg 9, 2629 HZ Delft, The Netherlands
[2] Present address: London Centre for Nanotechnology, University College London, London WCH1 0AW, UK
[3] Present address: Institute of Science and Technology Austria, 3400 Klosterneuburg, Austria
[*] These authors contributed equally to this work.
[†] Correspondence: t.idema@tudelft.nl
[**] Correspondence: g.h.koenderink@tudelft.nl

I. THEORETICAL MODEL OF EQUILIBRIUM SHAPES OF DUMBBELL VESICLES

As described in the main text, we assume that a dumbbell GUV is created of two vesicles, a larger outer one containing a smaller inner one, of which the inner one has burst, resulting in a shape with two lobes: one with a single and the other with a double membrane bilayer (Fig. S1). Here we study the shape of these dumbbells. Our approach is motivated by earlier theoretical work on domain-induced budding of vesicles composed of phase-separating lipid mixtures [1–4]. First we explain why the dumbbell shape can be described by two spherical caps, and second we explain how we infer the ratio between line tension and vesicle pressure from the shape of the GUV.

The shape energy of a GUV with negligible bending energy is given by [2]:

$$\mathcal{H} = \oint_{\partial 1} \sigma \, \mathrm{d}l + \Sigma^{(1)} A^{(1)} + \Sigma^{(2)} A^{(2)} + PV \, . \tag{S1}$$

The first term in Eq. (S1) describes the energy associated with the perimeter of the interface between the double bilayer surface and the single bilayer surface. Therefore, the integral runs along the edge of this interface, where σ is the line tension. The second and the third term correspond to the membrane tension, where A_i is the surface area and $\Sigma^{(i)}$ is the membrane tension of domain i, with $i = 1$ for the double membrane and $i = 2$ for the single membrane domain. The fourth term introduces a volume constraint, where P is the pressure difference $P = P_{\mathrm{ex}} - P_{\mathrm{in}}$ between the outside and the inside of the GUV and V is the volume of the GUV.

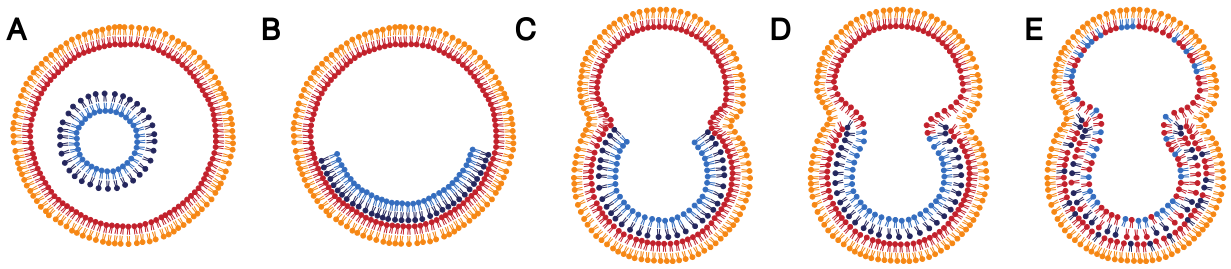

FIG. S1. **Schematic of dumbbell vesicle formation from nested GUVs.** (A) During GUV formation, nested vesicles are created. The leaflets of the outer GUV are shown in orange (outer) and red (inner) and the leaflets of the inner GUV are shown in black (outer) and blue (inner). (B) After the inner vesicle bursts, it leaks its entire volume into the GUV. (C) The membrane of the inner vesicle merges along its edge with the outer GUV. (D) The membranes of the inner vesicle and the outer GUV undergo hemifusion. (E) The lipids within the same membrane leaflet mix. At the interface, where the double bilayer and single bilayer meet, a line tension emerges that leads to the formation of a dumbbell vesicle.

We consider the limiting case where the energy associated with the line tension and the volume constraint dominate the system, and thus the contribution of the bending energy is negligible in Eq. (S1). This assumption can be justified by estimating the various energy contributions based on typical parameter values. For simplicity, we consider a sphere with radius $10\,\mu$m, which is the limiting case of a dumbbell with equal cap sizes and maximum opening angles. We assume a pressure difference of $P \sim 0.02\,\mathrm{Nm}^{-2}$ [3], a membrane tension of $\Sigma \sim 10^{-7}\,\mathrm{Nm}^{-1}$ [3] (neglecting differences between the two half spheres), a line tension of $\sigma \sim 1\,\mathrm{pN}$ [3] and a bending rigidity of $\kappa \sim 10^2\,\mathrm{pN\,nm}$ [3]. Using

Eq. (S1) and the bending energy of two half spheres, one with a double bilayer lobe and one with a single bilayer lobe ($8\pi\kappa + 4\pi\kappa$), we get: $E_{\text{pressure}} \sim 80\,\text{nN nm}$, $E_{\text{tension}} \sim 100\,\text{nN nm}$, $E_{\text{line}} \sim 60\,\text{nN nm}$ and $E_{\text{bending}} \sim 4\,\text{nN nm}$. Since the bending energy is over an order of magnitude smaller than the other contributions, we can neglect the energy contribution of membrane bending.

Since dumbbell shapes are axisymmetric, we can parameterize them by a (trivial) rotation angle ϕ about the symmetry axis, and a contour length s along their shape, see Fig. S2. The shape and local orientation of the contour can then be described by the radial position $r(s)$ and the tangent angle $\Psi(s)$. These parameters satisfy the geometric constraint $\dot{r} = \cos\Psi$, with a dot denoting the derivative with respect to the arc length s. To enforce this constraint, we add a term $\gamma(\dot{r} - \cos\Psi)$ to the shape energy, where γ is a Lagrange multiplier. We can then write the shape energy as the integral over an energy density

$$\begin{aligned}\mathcal{H} = \oint_{\partial 1} \sigma \,\mathrm{d}l + 2\pi \int_{s_0}^{s_1} \left[\Sigma^{(1)} r(s) + \frac{1}{2} P r^2 \sin\psi(s) + \gamma\left(\dot{r} - \cos\psi(s)\right)\right] \mathrm{d}s \\ + 2\pi \int_{s_1}^{s_2} \left[\Sigma^{(2)} r(s) + \frac{1}{2} P r^2 \sin\psi(s) + \gamma\left(\dot{r} - \cos\psi(s)\right)\right] \mathrm{d}s. \end{aligned} \tag{S2}$$

We can minimize the energy density within each domain, which gives us the following shape equations [2]:

$$0 = \frac{1}{2} P r^2 \cos\psi + \gamma \sin\psi, \tag{S3a}$$

$$\dot{\gamma} = \Sigma^{(i)} + P r \sin\psi, \tag{S3b}$$

$$\dot{r} = \cos\psi. \tag{S3c}$$

Moverover, we get a matching condition at the boundary ($s = s_1$), where there is a jump in the tangent angle ψ:

$$\lim_{\varepsilon \downarrow 0} \left[\gamma(s_1 + \varepsilon) - \gamma(s_1 - \varepsilon)\right] = \sigma. \tag{S4}$$

The spherical caps can be parametrized by $\psi(s) = s/R_i$ and $r(s) = R_i \sin(s/R_i)$. We solve Eq. (S3a) for γ, using the parametrization of the spherical caps, take the derivative with respect to s and use the resulting expression in Eq. (S3b). As a result, we find an equation for the pressure difference P and the Lagrange multiplier γ.

$$P = -\frac{2\Sigma^{(i)}}{R_i}, \tag{S5}$$

$$\gamma = -\frac{1}{2} P R_i^2 \sin\psi\cos\psi = \Sigma^{(i)} R_i \sin\psi\cos\psi \tag{S6}$$

Hence, if P and γ fulfill Eqs. (S5)-(S6), the dumbbell shape necessarily fulfills Eqs. (S3)-(S4). Therefore, the dumbbell shape is a minimal energy shape (with the boundary condition defined through Eq. (S4)), as previously noted by Baumgart et al. [3] or Allain and Ben Amar [4].

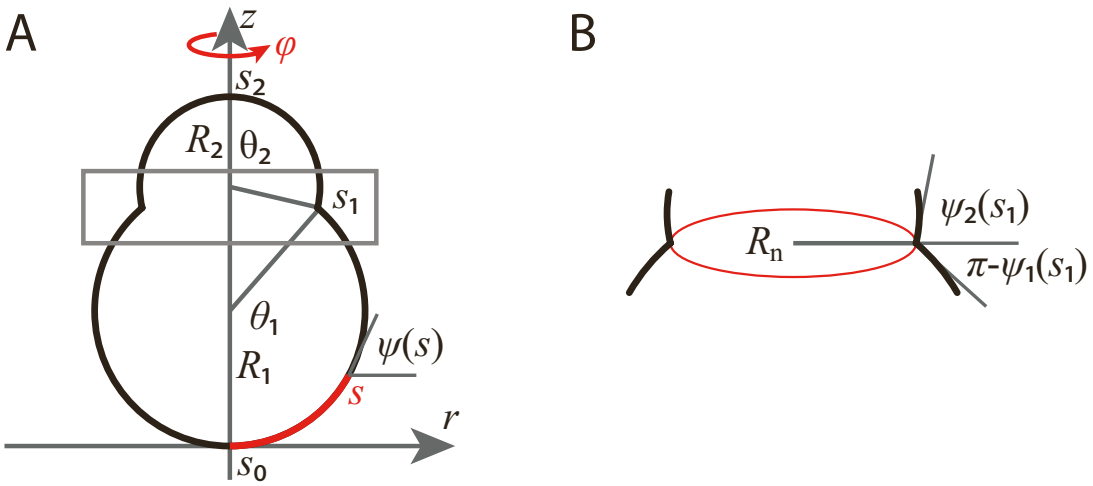

FIG. S2. **Geometry of dumbbell GUVs.** (A) Parametrization of the dumbbell shape by the arc length s (red) along the (rotationally symmetric) membrane contour. We take $s_0 = 0$ at the south pole of the dumbbell. The local orientation of the membrane is given by the angle $\psi(s)$. The bright and dim lobes are spherical caps characterized by their radii R_1 and R_2 and their opening angles at the neck, θ_1 and θ_2. The neck is located at $s = s_1$, and the north pole at $s = s_2$. (B) Zoom-in to the dumbbell neck region (grey rectangle, panel A). The line tension of the hemifusion line (red) determines the neck radius R_n. Dumbbell lobes connect to the plane of the neck at angles $\pi - \psi_1$ and ψ_2, respectively.

Eq. (S5) is the well-known Laplace pressure, relating the pressure difference across the membrane to the membrane's surface tension. Eq. (S6) gives us the value of the Lagrange multiplier γ in each domain. The two domains meet at the neck, where $R_1 \sin\theta_1 = R_2 \sin\theta_2 = R_\mathrm{n}$. Using the expressions for γ in the matching condition, Eq. (S4), with $\psi_1 = \theta_1$ and $\psi_2 = \pi - \theta_2$, allows us to calculate the ratio between the line tension σ and the pressure gradient P [3, 5]:

$$\frac{\sigma}{P} = \frac{1}{2} R_\mathrm{n}^2 \left(\cot\psi_1 - \cot\psi_2\right) = \frac{1}{2} R_\mathrm{n}^2 \left(\cot\theta_1 + \cot\theta_2\right) \tag{S7}$$

Fig. S3 shows the histogram of the ratio σ/P (blue) calculated from the measured GUV dumbbell shapes (cf. main text Fig. 4 G,H), according to Eq. (S7). Here, the opening angles of the bright and dark lobe of the dumbbell GUV, θ_1 and θ_2, are calculated from the diameters of the bright and dim lobe and the neck diameter of the GUV. The mean of the histogram (red) is at $-21\,\mu\mathrm{m}^2$, which is about half of the measured value for a vesicle that undergoes domain-induced budding ($-49\,\mu\mathrm{m}^2$) [3]. We note that the value of the ratio σ/P is negative because the (positive) pressure within the vesicle surmounts the pressure in the environment so that the pressure difference P is negative.

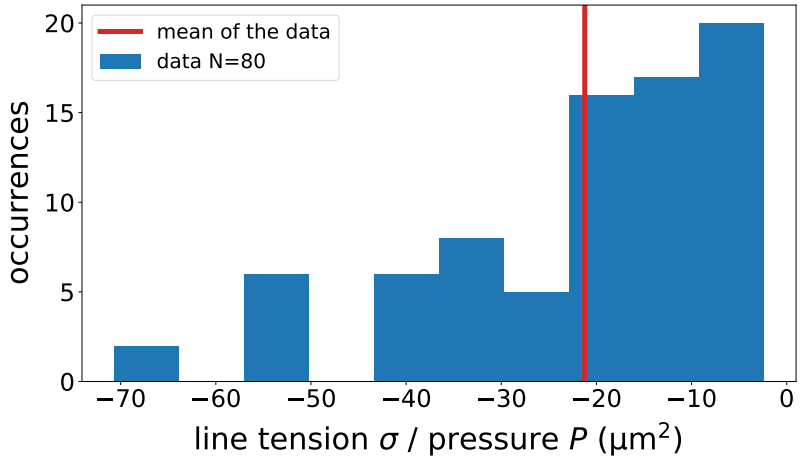

FIG. S3. Histogram of the line tension σ divided by the GUV pressure difference P calculated from the measured GUV dumbbell shapes (main text Fig. 4 G,H), according to Eq. (S7).

II. MODELING THE FORMATION OF DUMBBELL SHAPED GUVS

In the model, the total membrane area (the surface area plus excess membrane area) of the bursting vesicle A_v equals the surface area of the double bilayer membrane lobe A_1, i.e. $A_\mathrm{v} = A_1$. In addition, the GUV's total membrane area A_tot minus the surface area of the bursting lobe A_1 equals the surface area of the single bilayer membrane lobe A_2, i.e., $A_\mathrm{tot} - A_1 = A_2$ (Fig. 4 B of the main text). We calculated the radius of the bright lobe, R_1, from the total membrane area of the bursting vesicle, A_v,

$$R_1(\theta_1, A_\mathrm{v}) = \sqrt{\frac{A_\mathrm{v}}{2\pi(1-\cos\theta_1)}}\,, \tag{S8}$$

where θ_1 is the opening angle of the spherical cap. Similarly, we calculated the radius of the dim lobe, R_2,

$$R_2(\theta_2, A_\mathrm{v}, A_\mathrm{tot}) = \sqrt{\frac{A_\mathrm{tot} - A_\mathrm{v}}{2\pi(1-\cos\theta_2)}}\,, \tag{S9}$$

where θ_2 is the opening angle of the spherical cap. The two caps are connected at a circular interface with neck radius

$$R_\mathrm{n} = R_1 \sin\theta_1 = R_2 \sin\theta_2 \quad \rightarrow \quad R_2 = R_1 \frac{\sin\theta_1}{\sin\theta_2}\,. \tag{S10}$$

By equating Eq. (S9) with Eq. (S10) we obtain

$$\cos\theta_2(\theta_1, A_\mathrm{v}, A_\mathrm{tot}) = \frac{A_\mathrm{v}}{A_\mathrm{tot} - A_\mathrm{v}}\,(1+\cos\theta_1) - 1\,. \tag{S11}$$

The total volume of the GUV is given by adding up the volumes of the spherical caps of the bright and dark lobe

$$V(R_1, R_2, \theta_1, \theta_2) = \frac{\pi}{3} R_1^3\,(2+\cos\theta_1)\,(1-\cos\theta_1)^2 + \frac{\pi}{3} R_2^3\,(2+\cos\theta_2)\,(1-\cos\theta_2)^2\,. \tag{S12}$$

By substituting Eqs. (S8), (S9) and (S11) in Eq. (S12), we got an expression for the volume $V = V(\theta_1, A_\mathrm{tot}, A_\mathrm{v})$ of the GUV that only depends on θ_1, A_tot and A_v.

To connect the shape description derived above to the experiments, we calculated the geometrical correlations between the diameter of the bright and dim lobes from experimental data. First, we assumed that in the model, similar to the experiments, GUVs are created with excess membrane area that allows the GUV to change shape at constant volume. Therefore, the total membrane area A is larger than the surface area $A_\mathrm{s} = 4\pi R^2$, where R is the radius of the spherical GUV. In this case, the reduced area is given by $\nu = A/A_\mathrm{s}$, which varies across GUVs. Next, we sampled two radii $R_\mathrm{tot}, R_\mathrm{v}$ from the measured diameter distribution of GUVs (Fig. 1 C of the main text) that represent the sizes of the outer vesicle and the enclosed vesicle, respectively. From the radii $R_\mathrm{tot}, R_\mathrm{v}$ and the reduced areas $\nu_\mathrm{tot}, \nu_\mathrm{v}$ we calculated the GUV total membrane area,

$$A_\mathrm{tot} = 4\pi R_\mathrm{tot}^2 \nu_\mathrm{tot}\,, \tag{S13}$$

and the total membrane area of the enclosed vesicle,

$$A_\mathrm{v} = 4\pi R_\mathrm{v}^2 \nu_\mathrm{v}\,. \tag{S14}$$

We calculated the initial (spherical) GUV volume $V^* = 4\pi R_\mathrm{tot}^3/3$ and set V^* equal to the dumbbell volume obtained from Eq. (S12),

$$V(\theta_1, A_\mathrm{tot}, A_\mathrm{v}) = V^*\,. \tag{S15}$$

We solved Eq. (S15) for θ_1 by using the values of A_tot and A_v from Eqs. (S13) and (S14). With the value of θ_1 and the values of A_tot and A_v we could calculate the remaining quantities, where we determine θ_2, R_1, R_2 and R_n from Eqs. (S11), (S8), (S9) and (S10), respectively. Together, θ_1, θ_2, R_1, and R_2 define the GUV dumbbell shape.

III. SUPPLEMENTAL EXPERIMENTAL METHODS

A. Supplemental materials

Cholesterol (3β-Hydroxy-5-cholestene, 5-Cholesten-3β-ol, Cat. # C8667-1G) and sucrose (Cat. # S0389) were purchased from Sigma Aldrich. The following lipids were purchased from Avanti Polar Lipids: L-α-phosphatidylcholine (95 %) from chicken egg (EggPC), 1,2-dioleoyl-sn-glycero-3-phospho-L-serine (DOPS), 1,2-dioleoyl-sn-glycero-3-phospho-(1'-myo-inositol-4',5'-bisphosphate) (ammonium salt) (PIP_2), 1',3'-bis[1,2-dioleoyl-sn-glycero-3-phospho]-glycerol (sodium salt) (cardiolipin), and 1,2-dioleoyl-sn-glycero-3-phosphoethanolamine-N-(cap biotinyl) (biotin-PE). PIP_2 was stored in a mixture of chloroform, methanol and water at a 20:9:1 volumetric ratio, all other lipids were stored in chloroform and under argon at -20° C.

B. Supplemental microscopy methods

Widefield microscopy images were acquired on an inverted Leica Thunder Imager widefield microscope equipped with a 200 mW solid state LED5 light source, a 63x water immersion microscope (HC PL APO 63x / 1.20 W Corr CS2) and a monochrome sCMOS camera (Leica). Epifluorescence images were also acquired on an inverted Nikon Ti Eclipse microscope equipped with a 60x water immersion objective (CFI Plan Apochromat VC), a digital CMOS camera (Orca Flash 4.0), and an LED light source (Lumencor Spectra Pad X). Phase contrast images were acquired on the same Nikon Ti microscope using its DIA illuminator at a voltage of 12 V and using the corresponding phase mask in the microscope's condenser.

C. GUV production by gel-assisted swelling

Gel-assisted swelling of GUVs was performed following Ref. [6]. Cover glasses (22 x 22 mm, No. 1.5H, Paul Marienfield GmbH & Co. KG) were first rinsed with ethanol and MilliQ water and dried under a stream of nitrogen. They were then plasma cleaned for 30 seconds (PlasmaPrep III, SPI supplies), after which 100 μL of a solution of 5 % (w/v) polyvinyl alcohol (PVA, 145 kDA, 98 % hydrolysed, VWR, Amsterdam the Netherlands) in 200 mM sucrose in MilliQ water was spread over each coverslip at room temperature. The gel was solidified by baking it in an oven for 30 minutes at 50° C. Then, 10 μL of a lipid solution at a total lipid concentration of 1 mg/mL in chloroform, consisting of DOPC:Atto488-DOPE at a molar ratio of 99.5:0.5, was spread over the gel. The gel was placed in a vacuum desiccator for 30 minutes to ensure total evaporation of the organic solvent. The cover glasses were then placed in a compartmentalized petri dish (4 compartments, VWR), and to each gel we gently added 300 μL of GUV swelling buffer (10 mM Tris-HCl at pH 7.4, 100 mM KCl, 100 mOsm sucrose). After swelling for one hour, GUVs were collected by taking up the swelling solution with a pipette (1 mL tip), flushing the solution again over the cover slip once to dislodge the GUVs, and pipetting it up again.

D. GUV production by cDICE

cDICE GUVs were prepared from the same solutions and in the same rotating chamber as eDICE GUVs. Droplets were formed by injecting IAS into the oil phase at a rate of 25 μL/min for 5 min using a syringe pump (KDS 100 CE, KD Scientific). The capillary setup was identical to that described in [7].

E. Actin polymerization assays

Actin polymerization was quantified by the classical pyrene actin assay [8], following an existing protocol [9], briefly summarized below.

a. Hardware Pyrene assays were performed on a Duetta fluorescence and absorbance spectrometer (Horiba Scientific), equipped with an 80 W S/N 1344-DL lamp and TC1 temperature controller (Quantum Northwest). The temperature varied between 25.0 and 25.4 ° C. Measurements were performed following a custom-defined procedure in the Horiba EzSpec software. For an excitation wavelength of 365 nm, the emission at 407 nm was recorded for a 1 s integration time per data point. The excitation window was set at 10 nm and the emission window at 5 nm. These parameters were chosen to maximise the relative difference in intensity between polymerized and unpolymerized

pyrene-actin samples. All samples were measured in 3-window Quarz microvolume cuvettes from Hellma Analytics with an optical path length of 3 mm, holding 55 μL sample volumes. Cuvettes were cleaned by rinsing with 5 mL MilliQ water, 2 mL ethanol, and 2 mL MilliQ water between measurements, and dried under N_2 stream. Between different days of measurements, the cuvettes were further cleaned by sonicating in a 1 % Hellmanex solution for 5 min, sonicating for 5 min in MilliQ water to remove any excess detergent, and finally rinsing with 5 mL MilliQ water before drying under N_2 stream.

b. Procedure We performed all experiments in a final buffer with the same composition as the GUV IAS buffer, with at least two independent measurements per condition. Measurements with the different Arp2/3 isoforms but no Optiprep in the buffer were performed once per isoform. The final concentrations of actin, VCA and Arp2/3 complex were 4 μM, 650 nM, and 50 nM, respectively. We first prepared an actin premix to ensure a consistent starting concentration and labeling ratio of monomeric actin. It contained 95 % unmodified actin and 5 % pyrene-labeled actin, at 23.8 μM total, corresponding to 5.95 x the final actin concentration for the pyrene assay, in G-buffer. In the cuvette, the actin premix was then diluted into Mg-G-buffer (5 mM TrisHCl pH 7.4, 0.2 mM $MgCl_2$, 1 mM DTT, and 0.2 mM MgATP) and allowed to incubate for 2 min. In this step, Ca^{2+} ions on actin monomers are exchanged for Mg^{2+} ions, ensuring that actin polymerization commences at a reproducible starting point. Salts, Arp2/3 and VCA were then added and mixed by pipetting 5 times. The cuvette was placed in the spectrophotometer and the measurement was started, noting down the delay between adding salt and the first recorded data point (usually 10-15 s). The measurement was left to run until the fluorescence intensity plateaued.

c. Data analysis While the Duetta spectrometer offers simultaneous buffer measurement and correction, we chose to perform a manual background correction to increase time resolution of our measurements. This allowed us to acquire one datapoint per 1.1 s. For every measurement day, we first performed blank measurements on F-buffer and F-buffer including 6.5 % optiprep, where we repeated the same measurement 20 times. We then averaged these data points for every buffer individually, and subtracted the average from the sample data before further processing. To extract the time it takes to reach maximum pyrene fluorescence, as well as the actin elongation rate at the time where half of all G-actin is polymerized, we use a custom-written python script following the analysis laid out in [9]. We extract the time it takes each sample to reach maximum pyrene fluorescence and hence steady-state actin polymerization, as well as the actin elongation speed at the inflection point of the pyrene fluorescence curve. At this point, it is assumed half of all actin has polymerized and the increase in fluorescence intensity is only due to elongation, not nucleation [9].

IV. SUPPLEMENTAL FIGURES

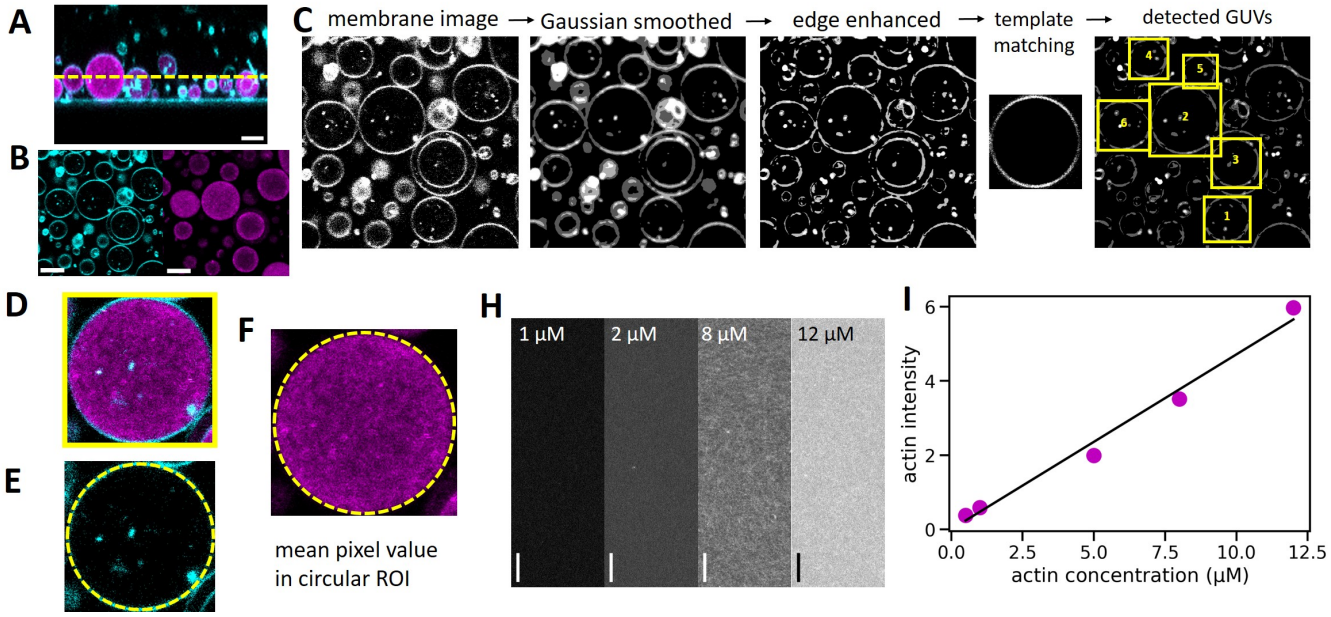

FIG. S4. **Quantifying actin concentrations.** (A) For quantitative confocal imaging, we performed an xz-scan to locate the precise z-position of the coverslip visible from its reflection (horizontal cyan line). Actin is shown in magenta, lipids in cyan. The yellow dashed line indicates a 7 μm height above the coverslip, where we took subsequent images. (B) Next, we acquired a two-channel xy-confocal image (actin in magenta, lipids in cyan). (C) We used an automated pipeline to detect the vesicles by pre-processing the images and subsequently locating GUVs using the template matching module in the DisGUVery toolbox [10]. Yellow boxes indicate the detected GUVs. (D) To extract the actin intensity inside a given GUV, we used the original unprocessed two-color image. We loaded each GUV detected by the template matching algorithm (here: GUV 2 from panel C) and drew a circular ROI of the same size as the template matching box ((E), yellow dashed circle). The mean pixel value inside this circular ROI in the actin channel was then taken as the average actin intensity of the GUV. To convert actin intensities into concentrations, we acquired a series of reference images of bulk actin networks (H) and constructed a concentration-intensity-calibration curve (I). Magenta datapoints represent the average mean pixel values of at least four 2048x2048 px reference images per condition, with standard deviations smaller than the data points. We fit the datapoints with a proportional model ($I_{\mathrm{act}}(c_{\mathrm{act}}) = A \cdot c_{\mathrm{act}}$, black line), which yields a proportionality constant of 0.471. Scale bars: 5 μm.

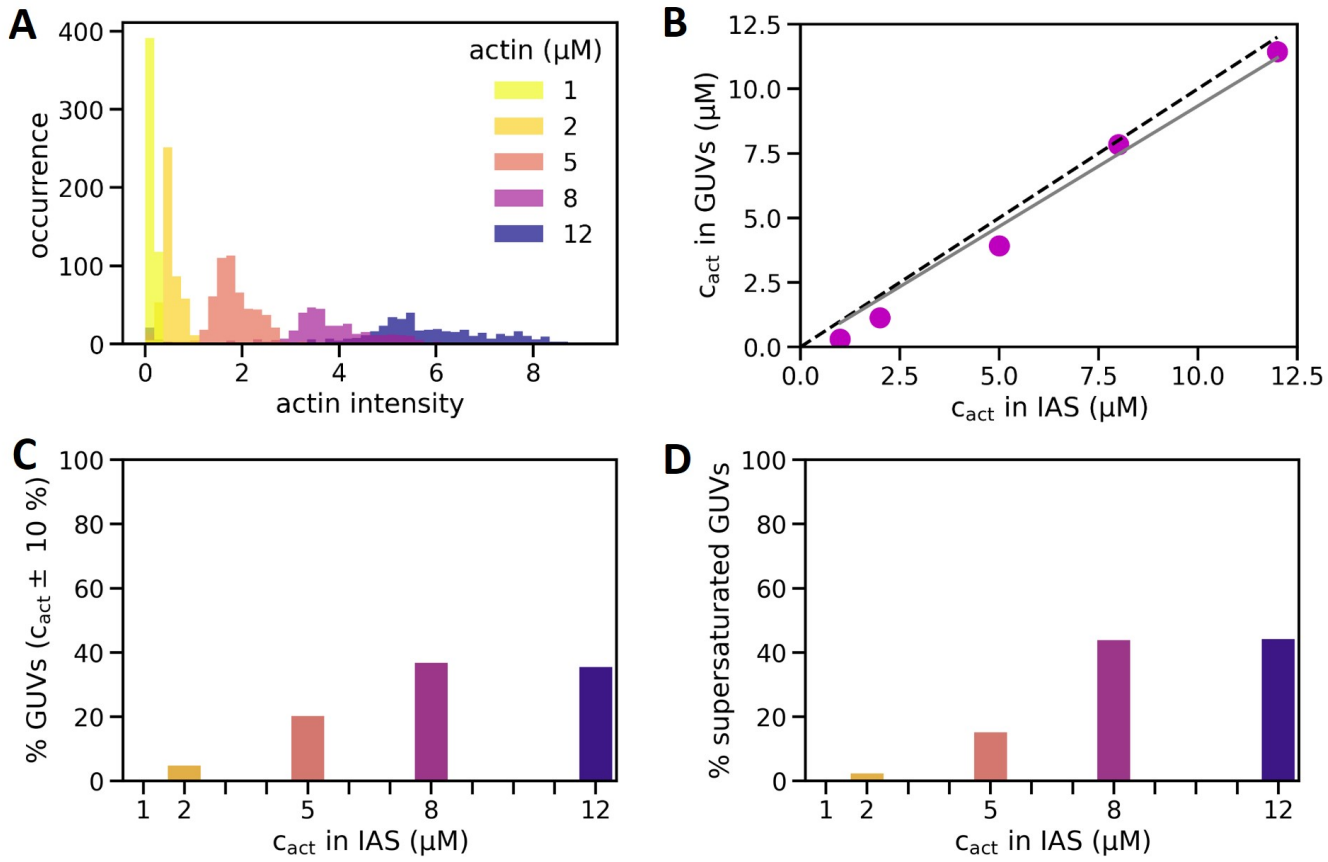

FIG. S5. **Extended quantification of actin encapsulation efficiency by eDICE.** (A) Histogram of actin intensities measured in individual GUVs by quantitative confocal microscopy. Darker colours indicate higher nominal actin concentrations. N = 2334 GUVs, with individual sample sizes N_i = 515, 468, 536, 368 and 447 GUVs for i = 1, 2, 5, 8, and 12 μM actin, respectively. (B) Mean actin concentration in the GUVs as a function of the nominal actin concentration in the inner aqueous solution. Magenta datapoints represent the mean of all GUVs at one nominal concentration (same sample sizes as in (A)), and the solid grey line indicates the proportional fit $c_{GUV}(c_{IAS}) = \xi \cdot c_{IAS}$, with $\xi = 93.3\%$. The dashed black line indicates perfect encapsulation, where the concentration in the GUVs equals the input concentration in the IAS. Error bars (95 % confidence interval on the mean) are not shown since they are smaller than the data points. (C) Bar plot showing the fraction of GUVs at different nominal actin concentrations containing actin at approximately the same concentration as the IAS (concentrations at $c_{nominal} \pm 10$ %). (D) Bar plot showing the fraction of GUVs that are significantly supersaturated in actin ($c_{GUV} > 1.1 \cdot c_{nominal}$).

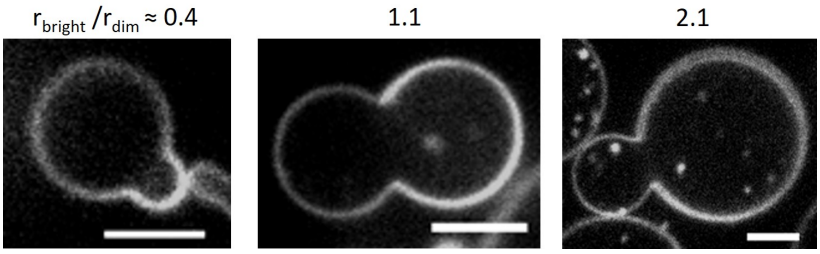

FIG. S6. **Dumbbell GUVs exhibit a range of shapes.** Most dumbbells had nearly equal sized lobes (middel panel, $r_{bright}/r_{dim} \approx 1$), but both significantly lower and higher size ratios also occurred (left and right panel, $r_{bright}/r_{dim} \approx 0.4$ and 2.1, respectively).

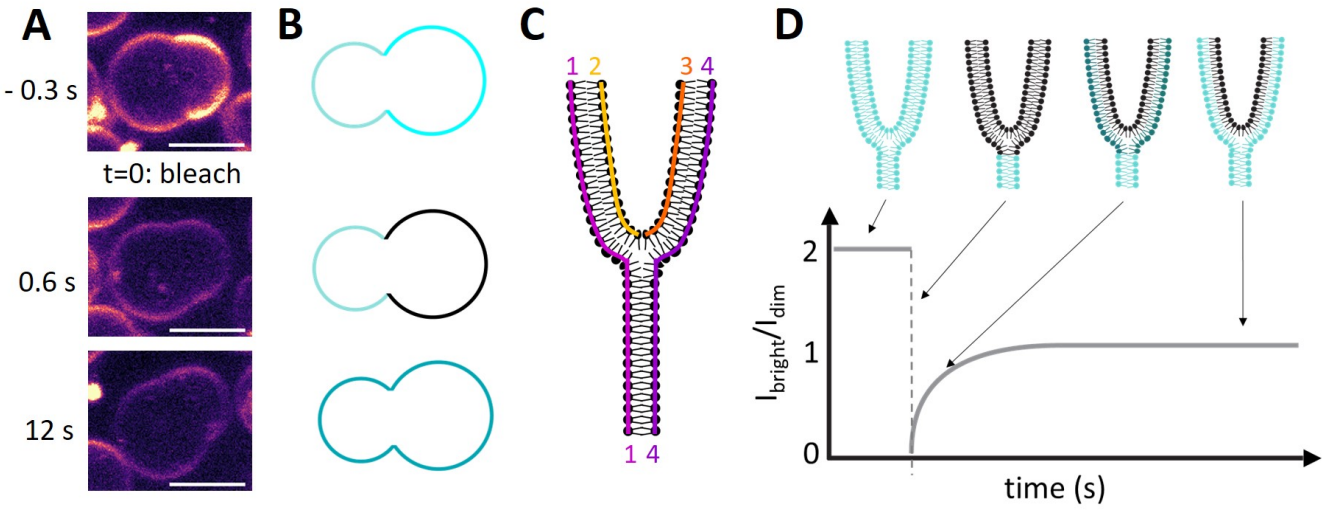

FIG. S7. **FRAP analysis to test a mechanism for dumbbell formation based on hemifusion of nested GUVs.** (A) Confocal images taken at the equatorial plane of a dumbbell-shaped GUV before and after bleaching the bright lobe. Scale bars: 5 μm. Membrane fluorescence is shown in false color (magma) for clarity. (B) Schematic of the bleaching experiment. The GUV starts out with a dim and a bright lobe (top). Ideally, all of the bright lobe's fluorescence gets bleached (middle). The remaining fluorescence from the unbleached lobe then redistributes in all connected leaflets of both lobes. (C) Schematic of the different lipid leaflets at the neck, assuming that the dumbbell shape results from hemifusion: leaflets 1 and 4 connect the dim and bright lobe, while leaflets 2 and 3 are disconnected and only span the bright lobe. Note that 'leaflets' 2 and 3 are two halves of one continuous monolayer of lipids that is bent in on itself, making it macroscopically appear as two separate leaflets. (D) Expected ideal recovery curve (bottom) and illustration of the fluorescence distribution in the different leaflets (top). Leaflets 2 and 3 (C) do not exchange lipids with leaflets 1 and 4, and consequently remain dark after bleaching. The intensity ratio between the bright and dim dumbbell lobes thus recovers not to 2, but to 1.

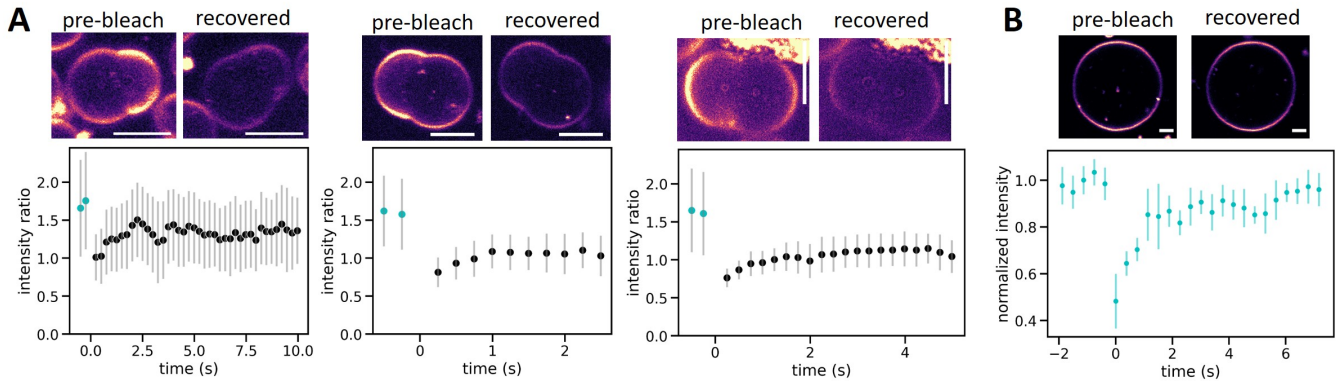

FIG. S8. **Extended FRAP data for dumbbell-shaped GUVs.** (A) Example FRAP curves for three additional dumbbells not shown in the main text. The bright lobe was bleached to approximately 30 % of its initial fluorescence intensity at t=0. The intensity ratio between the bright and the dim lobe consistently started out at around 1.7 (cyan data points), and recovered to between 1.0 and 1.4 within 2 s (black data points). (B) FRAP curve of a non-dumbbell GUV. Here, a 2x5 μm rectangular ROI at the top of the GUV was photobleached and the fluorescence recovery was monitored relative to a reference region on the opposite side of the GUV. The effect of photobleaching appeared more pronounced here than in the dumbbell GUVs, as we could bleach the small region much faster and were thus able to capture more of the initial recovery period. The fluorescence recovery timescale matched that seen in dumbbell GUVs (< 3 s). Confocal images above each graph show the equatorial slice of the GUV before photobleaching and after at least 15 s of recovery. Scale bars: 3 μm. Membrane fluorescence is shown in false color (magma) for clarity.

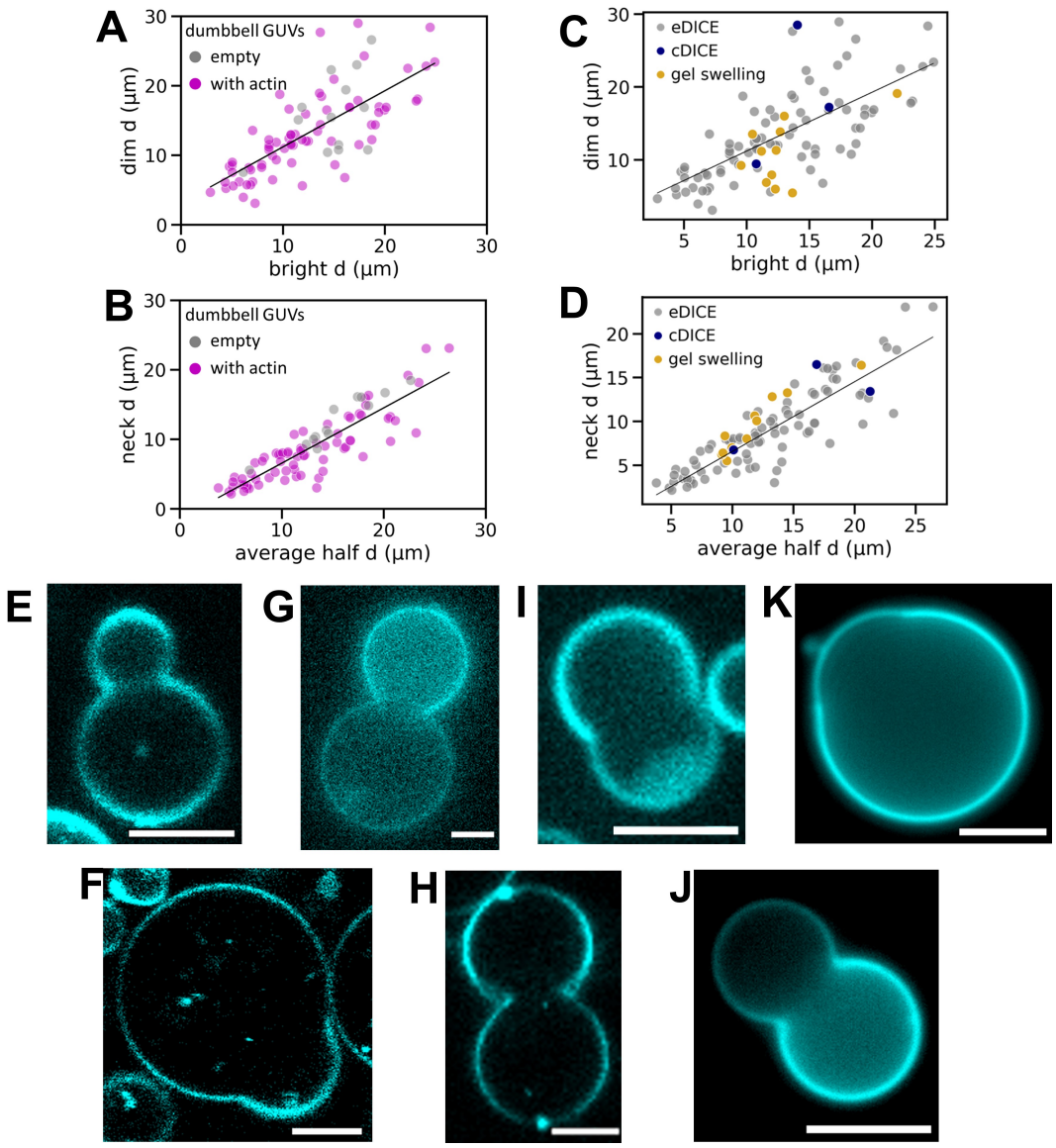

FIG. S9. **Dumbbell GUVs form for a range of IAS compositions and GUV production methods.** (A, B) Data from Fig. 4 H and I are re-plotted to show which dumbbells contain actin (magenta datapoints, either 4.4 or 8 μM actin in F-buffer, N = 72 GUVs) or only F-buffer (grey datapoints, N = 13). Actin does not appear to alter the formation of dumbbell shaped GUVs. (C, D) The shapes of dumbbells produced by cDICE (blue datapoints, N=3) and gel swelling (yellow datapoints, N=11) follow the same trends in relative lobe dimensions (C) and neck dimensions (D) as those produced by eDICE (grey datapoints, N=72). (E-L) Fluorescence microscopy images of dumbbell shaped GUVs produced in different circumstances. Dumbbells form in GUVs encapsulating only buffer (E), actin which polymerizes in the lumen without nucleating proteins (F), different concentrations of actin nucleated on the membrane by Arp2/3 and VCA (G: 4 μM actin, H: 8 μM actin), and with cortices where Arp2/3 driven actin nucleation is modulated by capping protein (I). (J) Dumbbell vesicles are also occasionally observed in samples produced by cDICE, in this case encapsulating G-buffer. (K) We even find dumbbells (albeit only rarely, < 2 %) when GUVs are produced by gel-assisted swelling and encapsulate only a sucrose solution. E, F, and H were acquired on a laser scanning confocal microscope; G and I were acquired on a spinning disk confocal microscope, and J and K were acquired on a Nikon epifluorescence microscope. Scale bars: 5 μm.

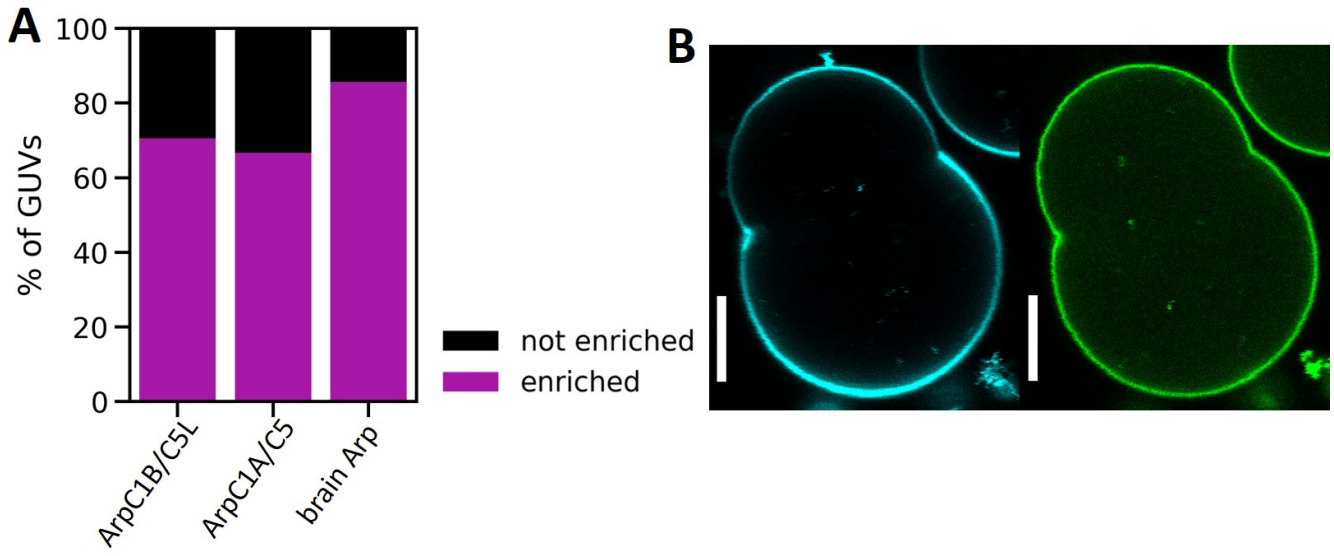

FIG. S10. **Actin was consistently enriched at the necks of dumbbell GUVs for different Arp2/3 isoforms, while VCA alone did not show enrichment.** (A) Bar plot showing the fraction of dumbbell GUVs in which actin was enriched at the neck, depending on the isoform of Arp2/3 which nucleates actin at the cortex. Actin and Arp2/3 were always at 8 μM and 50 nM, respectively, and VCA was either at 2 or 6.5 μM. Capping protein was absent. N = 17, 3 and 7 for Arp2/3 isoforms Arp2/3C1BC5L, Arp2/3C1AC5, and mixed isoforms isolated from porcine brain, respectively. While statistics for Arp2/3C1AC5 and brain Arp2/3are low, the data suggest that dendritic actin networks preferentially assemble at concave GUV neck regions for all these Arp2/3 isoforms. (B) Representative confocal image of a dumbbell GUV (membrane in cyan) encapsulating 6.5 μM fluorescent VCA (green). VCA covered the inner leaflet homogeneously, and we did not observe VCA enrichment at any of the 5 observed dumbbell necks.

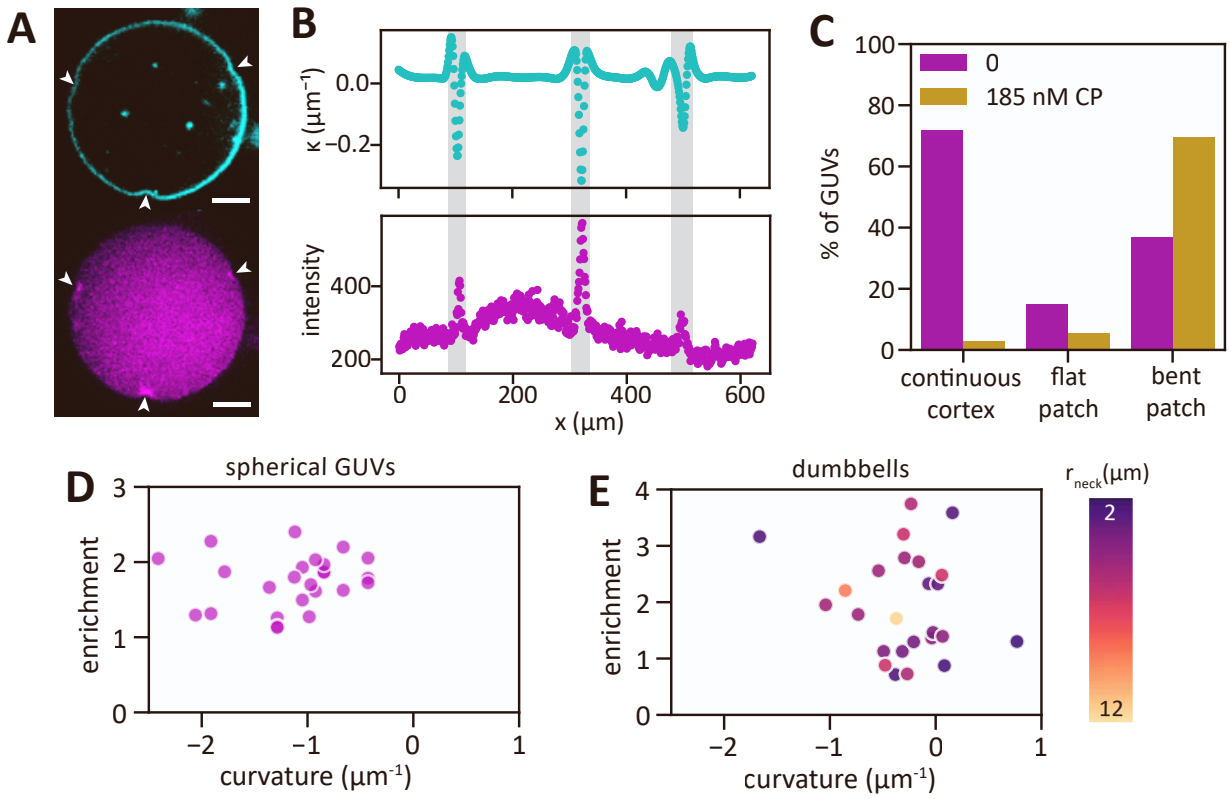

FIG. S11. **Branched actin networks associate with curved membrane regions in both spherical and dumbbell GUVs.** (A) Confocal slice of a GUV co-encapsulating 8 μM actin, 50 nM Arp2/3, 2.6 μM VCA and 185 nM capping protein. Actin (magenta) is enriched in small, bright, concave patches (white arrowheads) colocalized with bent sections of the GUV membrane (cyan). Scale bars: 5 μm. (B) Line profiles of the local membrane curvature (top) and actin signal intensity (bottom) along the GUV membrane in (A) confirm that spikes in actin signal occur at locations of negative membrane curvature (grey shaded regions). (C) Bar plot of the fraction of spherical GUVs with a continuous cortex, flat cortical patches, or bent cortical patches, for cortices without (magenta, N = 60 GUVs) or with (yellow, N = 36 GUVs) 185 nM capping protein. (D) Actin enrichment in bent patches as a function of patch curvature (N = 37 patches in 20 separate GUVs containing 185 nM capping protein). (E) Actin enrichment at dumbbell necks as a function of curvature. The data is color coded to reflect the 3D structure of the neck: darker colors indicate tighter necks with smaller r_{neck} (see color bar on the right). N = 27 dumbbell necks.

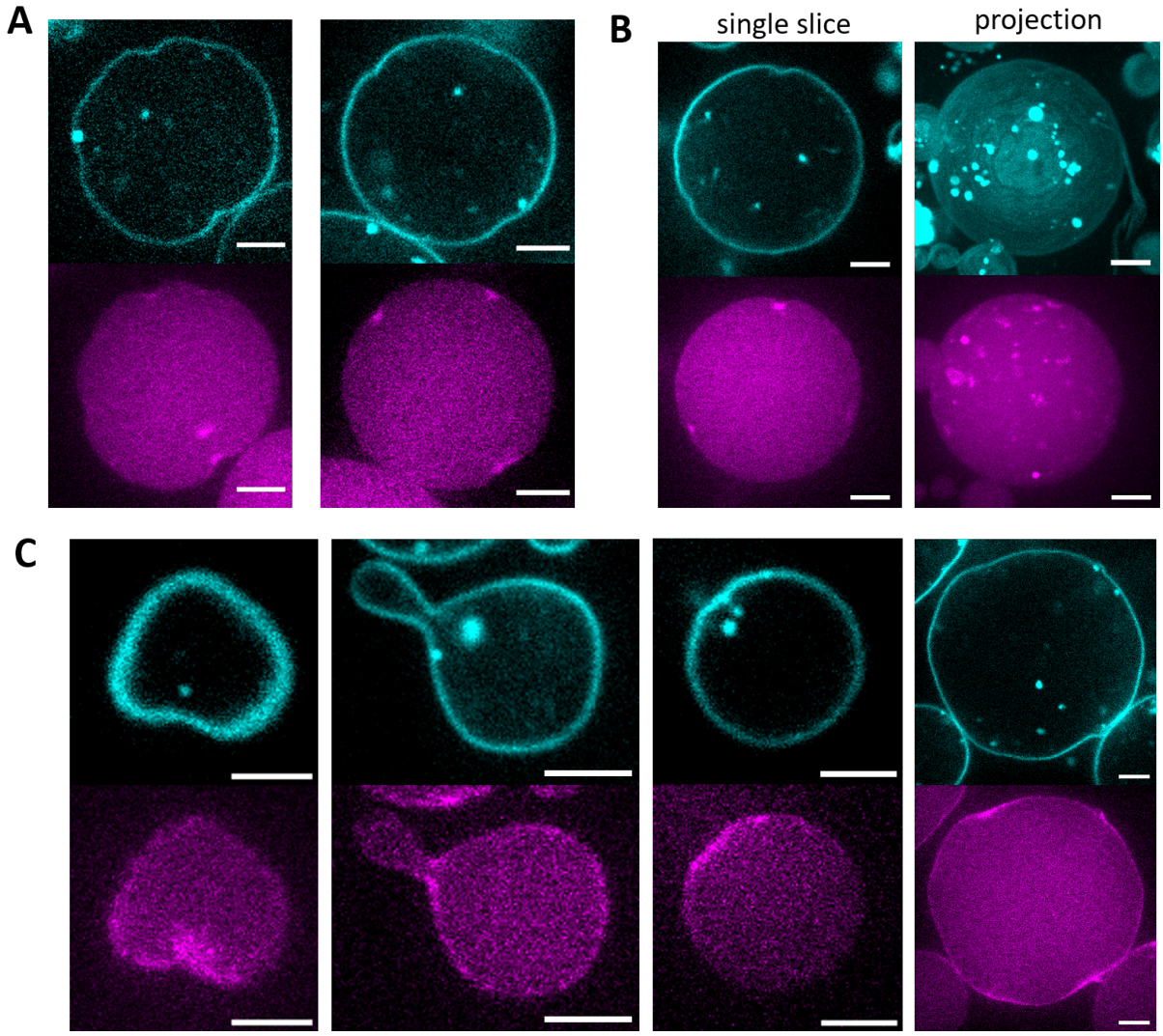

FIG. S12. **Concave actin patches in the presence of capping protein.** Confocal microscopy slices of two representative GUVs containing 8 μM actin, 50 nM Arp2/3 and 2.6 μM VCA, combined with 185 nM capping protein. Under these conditions, we observed small regions in which actin (magenta) was enriched at an inwardly bent membrane region (cyan). Typically, GUVs had a few (2-5) patches like the two examples shown in (A), but they could also bear many more concave patches spaced all around the GUV (B). The left and right panels in (B) show a single confocal slice and a maximum intensity projection of the same GUV, and all bright spots visible in the projection represent concave patches. (C) Confocal slices of GUVs with bent actin patches in GUVs with 8 µM actin, but no capping protein. Scale bars: 5 μm.

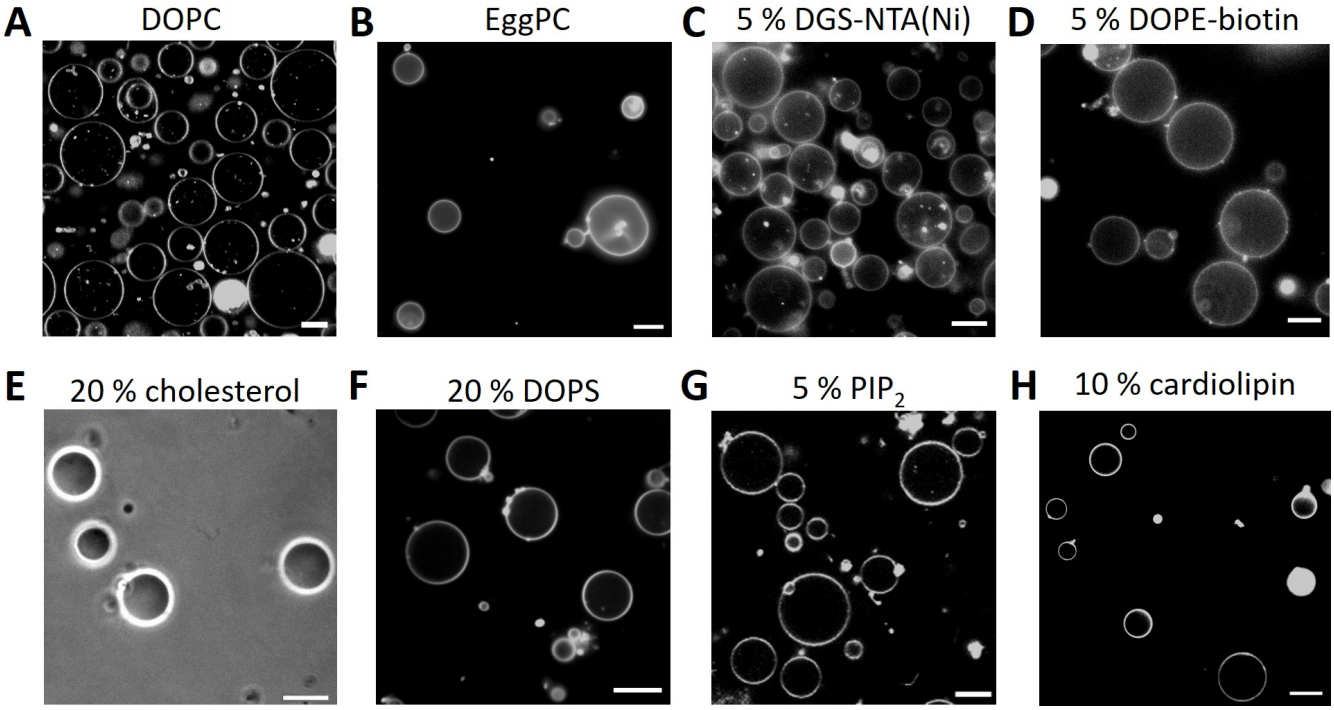

FIG. S13. **eDICE successfully produces GUVs with different lipid compositions.** (A) DOPC, (B) EggPC, (C) 95 % DOPC and 5 % DGS-NTA(Ni), (D) 95 % DOPC and 5 % biotin-DOPE, (E) 80 % DOPC and 20 % cholesterol, (F) 80 % DOPC and 20 % DOPS, (G) 95 % DOPC and 5 % PIP2, (H) 90 % DOPC and 10 % cardiolipin. (A) and (G) are confocal images acquired on the Stellaris LSCM, (B)-(D) and (H) are epifluorescence images acquired on the Nikon epifluorescence microscope, (E) was acquired on the same Nikon microscope in phase contrast mode, and (F) is a confocal image taken on the spinning disk confocal microscope. All GUVs except those shown in (E) are labeled with either 0.005 or 0.05 % of Cy5-DOPE. Scale bars: 10 μm.

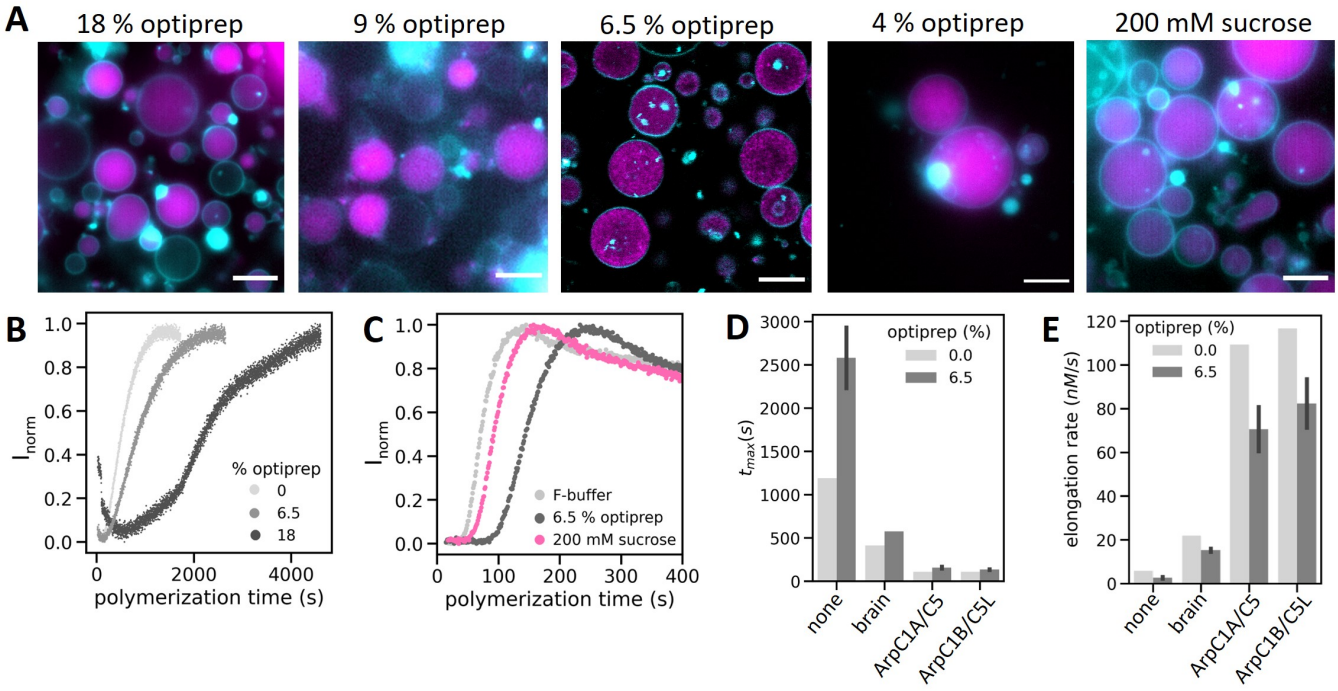

FIG. S14. **Effect of density gradient media on actin encapsulation and polymerization.** (A) Fluorescence images of GUVs encapsulating F-actin using different concentrations of density gradient media (see legends) in the IAS. The GUVs containing 6.5 % optiprep are shown as a single confocal slice, the other images show widefield images. Lipids are shown in cyan, actin in magenta. Scale bars: 10 μm. (B) Actin polymerization curves measured by pyrene fluorescence assay at different concentrations of Optiprep showed that optiprep interferes significantly with actin polymerization. (C) Pyrene actin polymerization curves indicate that sucrose used at a concentration compatible with eDICE also slowed actin polymerization dynamics, but to a lesser degree than Optiprep. (D) Bar plot of the time to reach steady state, $t_{\max}$ in the presence and absence of 6.5 % optiprep. (E) Bar plot of the actin elongation rate. Light grey bars in panels D and E represent one measurement in F-buffer, and dark grey bars represent the means of at least two separate measurements in F-buffer with optiprep, with error bars indicating the full spread of the data.

V. SUPPLEMENTAL TABLES

Compound	Instrument	Excitation	Detection
actin-AF488	Olympus spinning disk	491 nm laser, 10.5 %, 200 ms	Andor iXon X3 EM-CCD, gain 250
membrane-Cy5	Olympus spinning disk	640 nm laser, 53 %, 200 ms	Andor iXon X3 EM-CCD, gain 250
actin-AF488	Leica Stellaris LSCM	WLL at 499 nm, 18 %, 3.16 µs dwell time	HyDS2 (504-590 nm), counting mode
membrane-Cy5	Leica Stellaris LSCM	WLL at 640 nm, 2 %, 3.16 µs dwell time	HyDX3 (658-809 nm), counting mode
VCA-AF488C5	Leica Stellaris LSCM	WLL at 499 nm, 2 %, 3.16 µs dwell time	HyDX1 (510-567 nm), Standard mode, gain 60
actin-AF488	Nikon widefield	470 nm LED, 25 %, 200 ms	Hamamatsu Orca Flash 4.0
membrane-Cy5	Nikon widefield	640 nm LED, 30 %, 50 ms	Hamamatsu Orca Flash 4.0
actin-AF488	Leica widefield	475 nm LED, 5 %, 200 ms	sCMOS camera, gain 2
membrane-Cy5	Leica widefield	635 nm LED, 5 %, 50 ms	sCMOS camera, gain 2

TABLE S1. List of imaging settings. The left column lists the compound and their label, which is Alexa Fluor 488 (AF488) or Cy5. The 'Excitation' column shows the excitation wavelength, laser attenuation, and exposure time (camera-based microscopes) or pixel dwell time (confocal scanning microscope).

SUPPORTING REFERENCES

[1] F. Jülicher and R. Lipowsky, Domain-induced budding of vesicles, Physical Review Letters **70**, 2964 (1993).

[2] F. Julicher and R. Lipowsky, Shape transformations of vesicles with intramembrane domains, Physical Review E **53**, 2670 (1996).

[3] T. Baumgart, S. T. Hess, and W. W. Webb, Imaging coexisting fluid domains in biomembrane models coupling curvature and line tension, Nature **425**, 821 (2003).

[4] J. M. Allain and M. B. Amar, Budding and fission of a multiphase vesicle, European Physical Journal E **20**, 409 (2006).

[5] T. Baumgart, S. Das, W. W. Webb, and J. T. Jenkins, Membrane elasticity in giant vesicles with fluid phase coexistence, Biophysical Journal **89**, 1067 (2005).

[6] A. Weinberger, F. C. Tsai, G. H. Koenderink, T. F. Schmidt, R. Itri, W. Meier, T. Schmatko, A. Schröder, and C. Marques, Gel-assisted formation of giant unilamellar vesicles, Biophysical Journal **105**, 154 (2013).

[7] L. V. D. Cauter, F. Fanalista, L. V. Buren, N. D. Franceschi, E. Godino, S. Bouw, C. Danelon, C. Dekker, G. H. Koenderink, and K. A. Ganzinger, Optimized cdice for efficient reconstitution of biological systems in giant unilamellar vesicles, ACS Synthetic Biology **10**, 1690 (2021).

[8] J. A. Cooper, S. B. Walker, and T. D. Pollard, Pyrene actin: documentation of the validity of a sensitive assay for actin polymerization, Journal of Muscle Research and Cell Motility **4**, 253 (1983).

[9] L. K. Doolittle, M. K. Rosen, and S. B. Padrick, Measurement and analysis of in vitro actin polymerization, in *Adhesion Protein Protocols*, edited by A. S. Coutts (Humana Press, 2013) pp. 273–293.

[10] L. van Buren, G. H. Koenderink, and C. Martinez-Torres, Disguvery: A versatile open-source software for high-throughput image analysis of giant unilamellar vesicles, ACS Synthetic Biology **12**, 120 (2023).